Henry Yip
Student
s2231321@ed.ac.uk

Prof. J M Smillie
Supervisor
j.m.smillie@ed.ac.uk

SUMMER PROJECT ON THREE-BODY GRAVITATIONAL PROBLEM

Abstract. The Three-Body Problem involves three bodies, m_1, m_2, m_3, which attract each other according to Newton's law of inverse squares. While the two-body problem is well understood, the three-body problem is complex and far from fully solved. Since the 18th century, this problem has attracted the attention of some of the greatest mathematicians, such as Euler, Poincaré, Laplace, and Lagrange. With the advent of supercomputers, more and more classifications of orbits have been discovered.

In this report, we have two main goals. The first goal is to introduce and present some interesting orbits. We will attempt to verify and plot important results from various books and papers. The second goal is to understand some of the theoretical results developed in the last decade, especially the proof of Figure-8 orbits and the convergence of Sundman's series. We conclude this report by searching for well-behaved orbits.

Contents

Date: July 31, 2024.

1. Introduction and Mathematical Formulation

Below I will introduce the mathematical formulation behind the Three-Body Problem.

1.1. **Newton's Law of Universal Gravitation.** Knowing the separation $|\mathbf{r}_1 - \mathbf{r}_2|$ between any two bodies, we can calculate the total force acting on them ([8]):

$$\mathbf{F}_{12} = \frac{Gm_1m_2(\mathbf{r}_1 - \mathbf{r}_2)}{|\mathbf{r}_1 - \mathbf{r}_2|^3}.$$

Where G is the gravitational constant. Throughout the report, we will assume $G = 1$ for simplicity. This is a common convention [12].

Including the contribution of forces from other bodies, we obtain:

$$\mathbf{F}_i = \sum_{j \neq i} \mathbf{F}_{ij} = \sum_{j \neq i} \frac{Gm_im_j(\mathbf{r}_i - \mathbf{r}_j)}{|\mathbf{r}_i - \mathbf{r}_j|^3}.$$

1.2. **Newton's Second Law.** The force on each body relates to its acceleration by Newton's second law:

$$\mathbf{F}_i(t) = m_i\mathbf{a}_i(t),$$

where acceleration is defined by:

$$\mathbf{a}_i(t) = \frac{d\mathbf{v}_i}{dt}.$$

Given the velocity of a point mass for every time t, we can obtain the trajectory of the system. The main focus of this report is how the trajectory of the system varies with time.

2. Integration Methods for Numerical Simulation

Since the Three-Body Problem does not have a useful analytical form, much of the current research is based on numerical simulations. An integration method will be selected below, based on different criteria.

2.1. **Definition of order of an integration method.** Global error is the cumulative error over all steps compared to the exact solution of the differential equation [5]. An integration method has order n if the global error is of order $O(h^n)$, where h is the stepsize. For example, Euler Method has the form $y_{n+1} = y_n + hf(t_n, y_n)$. The global error is of order $O(h)$ and hence is of order 1. This means the global error decreases linearly with the step size h. Thus, the approximation becomes more accurate as h becomes smaller, with the cost of increased computational steps and computational time. To determine if an integration method is suitable, it is important to check if the conserved quantities, such as the total energy and linear momentum are conserved.

2.2. **Definition of a symplectic integrator.** This subsection is based on the report *Computer Implementation of Symplectic Integrators and Their Applications to the N-Body Problem* [2]. Conservation of energy can be achieved through symplectic integrators, where v and x are velocities and positions respectively:

$$v^{(i)} = v^{(i-1)} + c_i a(x^{(i-1)})dt$$
$$x^{(i)} = x^{i-1} + d_i v^{(i)}dt.$$

For compactness, we can express

$$\mathbf{A} = \begin{pmatrix} \mathbf{c} \\ \mathbf{d} \end{pmatrix}$$

where

$$\mathbf{c} = [c_1, c_2, ..., c_{i-1}, c_i]$$
$$\mathbf{d} = [d_1, d_2, ..., d_{i-1}, d_i].$$

It has been shown that the elements in $\mathbf{c}$ and $\mathbf{d}$ sum to 1.

It has also been shown that:

$$\mathbf{A} = \begin{pmatrix} 1 \\ 1 \end{pmatrix}$$

leads to a First-Order Symplectic Integration Method. This is the Euler Method.

Meanwhile

$$\mathbf{A} = \begin{pmatrix} \frac{1}{2} & \frac{1}{2} \\ 1 & 0 \end{pmatrix}$$

leads to a Second-Order Symplectic Integration Method. This is the Verlet Method. Also,

$$\mathbf{A} = \begin{bmatrix} \frac{7}{24} & \frac{3}{4} & \frac{-1}{24} \\ \frac{2}{3} & \frac{-2}{3} & 1 \end{bmatrix}$$

leads to a Third-Order Symplectic Integration Method. This will be referred to as the Ruth Method. At last,

$$\mathbf{A} = \begin{bmatrix} \frac{1}{2\left(2-2^{1/3}\right)} & \frac{1-2^{1/3}}{2\left(2-2^{1/3}\right)} & \frac{1-2^{1/3}}{2\left(2-2^{1/3}\right)} & \frac{1}{2\left(2-2^{1/3}\right)} \\ \frac{1}{2-2^{1/3}} & \frac{-2^{1/3}}{2-2^{1/3}} & \frac{1}{2-2^{1/3}} & 0 \end{bmatrix}$$

leads to a Fourth-Order Symplectic Integration Method. This will be referred to as the Neri method.

It is important to note that the velocity is always updated before the position. This is illustrated using the Ruth Method:

$$v^{(1)} = v^{(0)} + c_1 a(x^{(0)})dt$$
$$x^{(1)} = x^{(0)} + d_1 v^{(1)} dt$$
$$v^{(2)} = v^{(1)} + c_2 a(x^{(1)})dt$$
$$x^{(2)} = x^{(1)} + d_2 v^{(2)} dt$$
$$v^{(3)} = v^{(2)} + c_3 a(x^{(2)})dt$$
$$x^{(3)} = x^{(2)} + d_3 v^{(3)} dt.$$

The process will then be repeated over and over throughout the simulation.

2.3. **Metrics for choosing an integration method.** To choose the most suitable integration method, we will define several metrics to evaluate the precision of the numerical methods specified above. These metrics will be compared across three different orbits, namely the Figure-8 orbit, the Bumblebee Orbit, and the Moth Orbit. Each orbit will be simulated with a total of $100,000$ steps, using a step size of 0.0001.

The first metric is the energy deviation. It is defined in a document by Joe Zuntz as: [14]:

$$\frac{\Delta E}{E_0} = \left| \frac{E_{\max} - E_{\min}}{E_0} \right|$$

where E_0 is the energy at the start of the simulation. A good model requires:

$$\frac{\Delta E}{E_0} < 1.$$

The second metric is named the momentum difference. For many systems, the initial Momentum is zero. Therefore, Momentum Deviation cannot be well defined. Instead, we will only check the Momentum Difference, which can be defined as:

$$\text{Max } \Delta p_x = |p_{\max,x} - p_{\min,x}|$$
$$\text{Max } \Delta p_y = |p_{\max,y} - p_{\min,y}|.$$

The third metric is the run time. Run Time is important for particularly long simulations. In our case, most simulations are relatively short so it is not as important as the metrics above. Nonetheless, a faster simulation method is advantageous, provided that it does not compromise the quality of the output. Below I will compare different methods and pick the suitable one.

Method	**Energy Deviation**	**Max Δp_x**	**Max Δp_y**	**Run Time (s)**
Neri (Order 4)	6.124×10^{-14}	1.040×10^{-13}	4.852×10^{-14}	29.60
Ruth (Order 3)	1.280×10^{-13}	5.307×10^{-14}	3.048×10^{-14}	25.91
Verlet (Order 2)	5.893×10^{-9}	3.841×10^{-14}	2.232×10^{-14}	12.31
Euler (Order 1)	3.601×10^{-5}	3.686×10^{-14}	3.009×10^{-14}	15.53

TABLE 1. Comparison of Ruth, Neri, Verlet and Euler Methods (Figure-8 Orbit)

Method	**Energy Deviation**	**Max Δp_x**	**Max Δp_y**	**Run Time (s)**
Neri (Order 4)	8.058×10^{-3}	4.591×10^{-14}	9.246×10^{-14}	27.79
Ruth (Order 3)	8.058×10^{-3}	7.394×10^{-14}	4.249×10^{-14}	23.84
Verlet (Order 2)	9.676×10^{-2}	2.287×10^{-14}	1.882×10^{-14}	11.56
Euler (Order 1)	2.4329	3.625×10^{-14}	2.312×10^{-14}	15.71

TABLE 2. Comparison of Ruth, Neri, Verlet and Euler Methods (Bumblebee Orbit)

Method	**Energy Deviation**	**Max Δp_x**	**Max Δp_y**	**Run Time (s)**
Neri (Order 4)	1.459×10^{-9}	4.874×10^{-14}	8.693×10^{-14}	28.06
Ruth (Order 3)	2.143×10^{-8}	3.486×10^{-14}	3.185×10^{-14}	22.39
Verlet (Order 2)	4.775×10^{-5}	2.387×10^{-14}	3.835×10^{-14}	11.55
Euler (Order 1)	0.02070	2.031×10^{-14}	2.183×10^{-14}	13.76

TABLE 3. Comparison of Ruth, Neri, Verlet and Euler Methods (Moth Orbit)

It is somewhat surprising that the Verlet Method has the lowest running time, even lower than that of the Euler Method. More interestingly, the Verlet Method also conserves Momentum slightly better than methods with higher orders. However, the difference is too small to be significant (all of order 10^{-14}). It can be seen that the Neri Method conserves Energy much better than other methods, especially in the Moth Orbit simulation.

Even though the Neri method causes a significantly longer run time, it is not a significant limiting factor as most simulations are considerably short. Therefore, the Neri method will be chosen throughout this report.

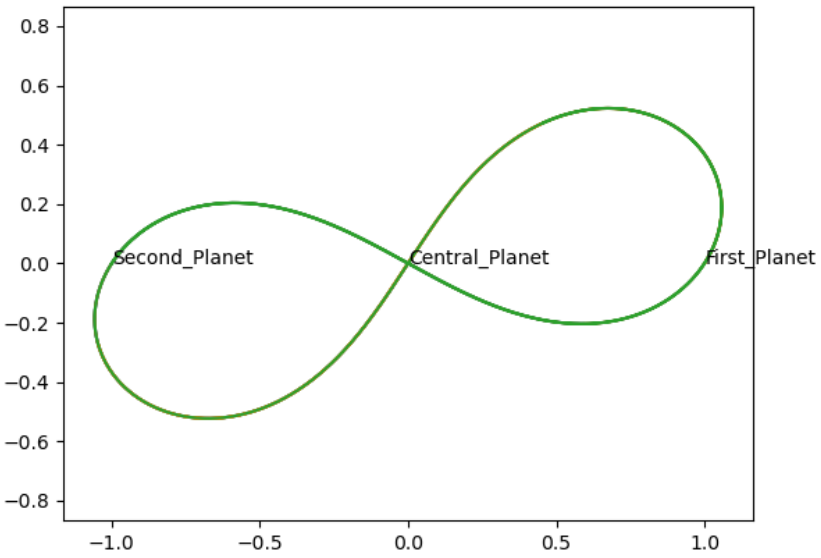

FIGURE 1. The Figure-8 Orbit.

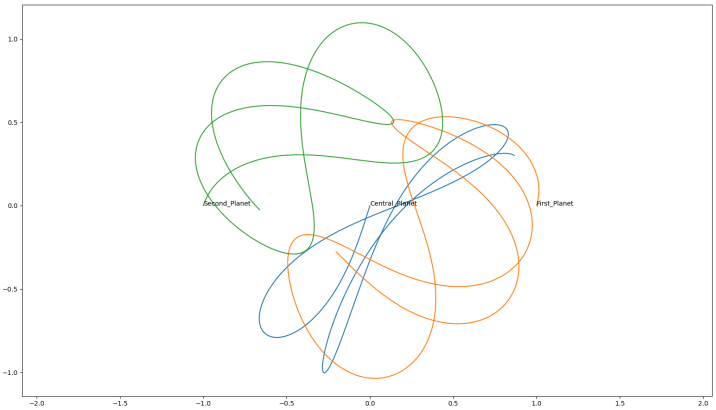

FIGURE 2. The Bumblebee Orbit.

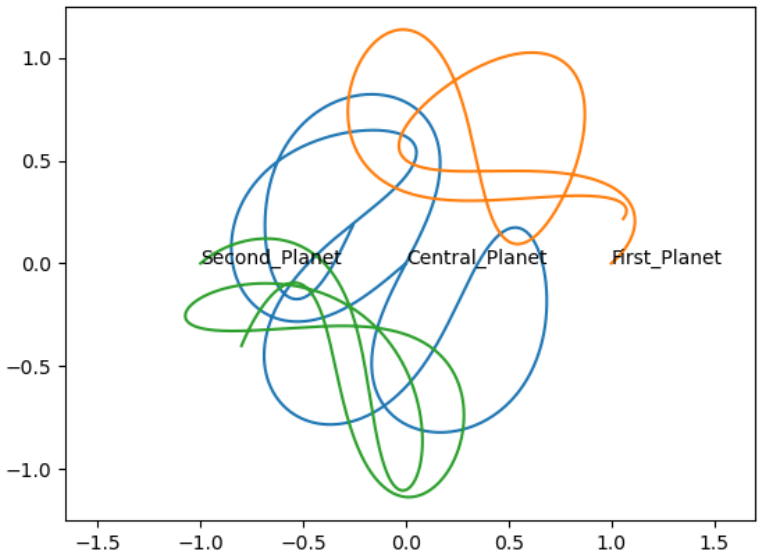

FIGURE 3. The Moth Orbit.

3. Euler's Restricted Three-body Problem

3.1. **Setup.** In this section, we mainly consider the setup in the book *Integrable Systems in Celestial Mechanics* [8], namely the Euler Problem. Consider the z-axis plotted against the x-axis. The two masses m_+ and m_- are located at $(0, 1)$ and $(0, -1)$ respectively whereas the third mass can move around freely. A plot can be seen in Figure (4). As two of the masses are stationary, this problem is also called the problem of two fixed centers.

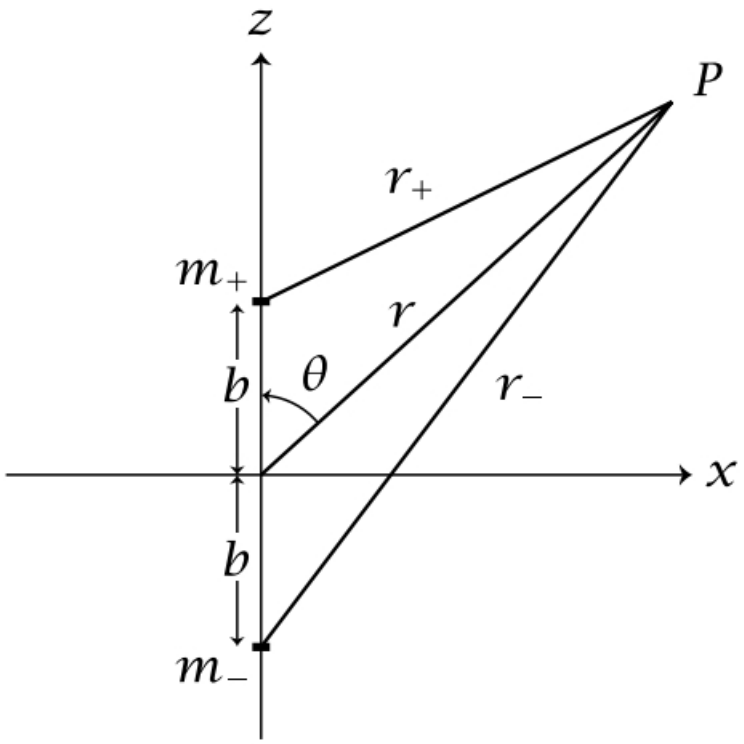

Figure 4. Setup of the Euler Problem.

It is stated in the book that it is a convention to express the system in terms of planar prolate spheroidal coordinates:

$$x = \pm\sqrt{R^2 - b^2}\sin\sigma$$
$$z = R\cos\sigma$$

where $R \in (0, \infty]$, $\sigma \in [0, \pi]$.
The advantage of this form is we can express:

$${r_+}^2 = (R - b\cos\sigma)^2$$
$${r_-}^2 = (R + b\cos\sigma)^2$$

3.2. **Expressing prolate spheroidal coordinates using cartesian coordinates.** As $x = \pm\sqrt{R^2 - b^2}\sin\sigma$, we notice that for $x < 0$, it has the identical R and σ values corresponding to $|x|$. Therefore without loss of generality, we can consider $x > 0$.

As $\cos\sigma$ is only negative in the range $\frac{\pi}{2} < \sigma < \pi$, we have $z > 0$ for $0 < \sigma < \frac{\pi}{2}$ and $z < 0$ for $\frac{\pi}{2} < \sigma < \pi$. We will consider these two cases separately.

3.2.1. *Case for $z > 0$.* Using $R = \frac{z}{\cos\sigma}$, we can substitute one of the equations into the other:

$$\begin{aligned} x &= \sin\sigma\sqrt{\left(\frac{z}{\cos\sigma}\right)^2 - 1} \\ &= \sqrt{\frac{z^2 - \cos^2\sigma}{\cos^2\sigma}}\sin\sigma \\ x^2 &= \frac{(z^2 - 1 + \sin^2\sigma)(\sin^2\sigma)}{1 - \sin^2\sigma} \\ x^2 &= \sin^2\sigma(x^2 + z^2 - 1 + \sin^2\sigma), \end{aligned}$$

where we have used $\cos\sigma = \sqrt{1 - \sin^2\sigma}$. This is valid as $0 < \sigma < \frac{\pi}{2}$. By letting $u = \sin^2\sigma$, we have:

$$u^2 + (x^2 + z^2 - 1)u - x^2 = 0.$$

Using the Quadratic Formula, and noting that $\sqrt{u} = \sin\sigma$, we arrive at

$$\arcsin\sqrt{u} = \sigma_{z>0},$$

where

$$u = \frac{-(x^2 + z^2 - 1) + \sqrt{(x^2 + z^2 - 1)^2 + 4x^2}}{2}.$$

3.2.2. *Case for $z < 0$.* We have assumed $x > 0$ and found the solution for $z > 0$. Now we want to find the solution for $z < 0$ while keeping $x > 0$.

Note that $\sin(\pi - \sigma) = \sin\sigma$ and $\cos(\pi - \sigma) = -\cos\sigma$. As $x \propto \sin\sigma$ and $z \propto \cos\sigma$, by letting $\sigma_{z<0} = \pi - \sigma_{z>0}$, we can find solutions for $z < 0$.

To summarize:

$$\sigma = \begin{cases} \arcsin\sqrt{u} & \text{for } z > 0, \\ \pi - \arcsin\sqrt{u} & \text{for } z < 0, \end{cases}$$

where

$$u = \frac{-(x^2 + z^2 - 1) + \sqrt{(x^2 + z^2 - 1)^2 + 4x^2}}{2}.$$

Finding R is very straightforward given σ and hence is omitted.

3.3. **Lagrangian of the System.**

3.3.1. *Definition of the Lagrangian.* Lagrangian mechanics is a formulation of classical mechanics. The Lagrangian, denoted as $\mathcal{L}$, can be expressed as [11]:

$$\mathcal{L} = T - V.$$

Where T is the kinetic energy and V is the potential energy. The Equations of Motions can be obtained through:

$$\frac{\partial\mathcal{L}}{\partial q} - \frac{d}{dt}\left(\frac{\partial\mathcal{L}}{\partial\dot{q}}\right) = 0 \quad \text{(Euler-Lagrange Equation)}$$

where q is a generalized coordinate. As this is a two-dimensional system, there are two generalized coordinates. The Lagrangian will be used in later parts of this report, in the form of the Principle of Least Action.

3.3.2. *Kinetic Energy.* As we have:

$$\mathbf{r}(R,\sigma) = \begin{pmatrix} x(R,\sigma) \\ z(R,\sigma) \end{pmatrix}$$

We can deduce:

$$\frac{\partial x}{\partial R} = \pm\frac{R\sin\sigma}{\sqrt{R^2-b^2}}, \quad \frac{\partial z}{\partial R} = \cos\sigma$$

$$\frac{\partial x}{\partial \sigma} = \pm\sqrt{R^2-b^2}\cos\sigma, \quad \frac{\partial z}{\partial \sigma} = -R\sin\sigma$$

We can thus calculate the partial derivatives:

$$\mathbf{r}_R = \frac{\partial \mathbf{r}}{\partial R} = \begin{pmatrix} \frac{R\sin\sigma}{\sqrt{R^2-b^2}} \\ \cos\sigma \end{pmatrix}$$

$$\mathbf{r}_\sigma = \frac{\partial \mathbf{r}}{\partial \sigma} = \begin{pmatrix} \sqrt{R^2-b^2}\cos\sigma \\ -R\sin\sigma \end{pmatrix}$$

and calculate the metric components using:

$$g_{RR} = \mathbf{r}_R \cdot \mathbf{r}_R$$

and so on.
Doing this process three times will lead us to:

$$g_{RR} = \frac{R^2-b^2\cos^2\sigma}{R^2-b^2}, \quad g_{R\sigma} = 0, \quad g_{\sigma\sigma} = R^2 - b^2\cos^2\sigma.$$

3.3.3. *Potential Energy.* We can express the potential energy V:

$$V = -\mu\frac{R+\beta b\cos\sigma}{R^2-b^2\cos^2\sigma}$$

with

$$\beta = \frac{m_+ - m_-}{m_+ + m_-}.$$

The details of the proof are less illuminating and therefore will be skipped. As we have expressions for both T and V, we can obtain:

3.3.4. *Lagrangian of the system.*

$$\begin{aligned}\mathcal{L} &= T - V \\ &= \frac{1}{2}\frac{R^2-b^2\cos^2\sigma}{R^2-b^2}\dot{R}^2 + \frac{1}{2}\left(R^2-b^2\cos^2\sigma\right)\dot{\sigma}^2 + \mu\frac{R+\beta b\cos\sigma}{R^2-b^2\cos^2\sigma}\end{aligned}$$

Equations of motions of R and σ can be obtained by solving the Euler-Lagrange Equation.

3.4. **Listing the conserved quantities.** In this subsection, we discuss the conserved quantities in the setup. This is important for classifying orbits in later parts of the report. First, we will state two quantities that are not conserved.

3.4.1. *Linear Momentum and Angular Momentum are not conserved.* Both linear momentum and angular momentum are not conserved as two of the bodies are fixed in place, implying the existence of external forces. This can be illustrated by releasing a point mass a distance away from the two fixed bodies. The initial momentum and linear momentum are zero but the point mass is attracted by the two fixed bodies and accelerates towards them. This leads to a non-zero linear momentum and angular momentum over time.

Below we describe quantities that are conserved.

3.4.2. *Energy is conserved.* The kinetic energy of the moving point mass is converted to the potential energy between itself and the two fixed masses. There is no energy lost.

3.4.3. *g and h - constants that define type of orbit, are conserved [4].* This is slightly modified from the cited paper due to a different set-up:

$$g = \frac{1}{2}\left(zp_x - xp_z\right)^2 + \frac{1}{2}d^2p_z^2 + dz\left(\frac{m_1}{\sqrt{(z+d)^2+x^2}} - \frac{m_2}{\sqrt{(z-d)^2+x^2}}\right)$$
$$h = \frac{1}{2}\left(p_z^2 + p_x^2\right) - \frac{m_1}{\sqrt{(z+d)^2+x^2}} - \frac{m_2}{\sqrt{(z-d)^2+x^2}},$$

where d is the distances of the two centers from the origin. Both g and h will be used to determine the type of orbit. Note that h is simply the energy of the third particle.

3.4.4. *C_1 and C_2 - constants that define eccentricity and semi-major axis or some orbits, are conserved.* These two additional conserved quantities are denoted in the book mentioned in the early parts of this section [8]:

$$\frac{1}{2}\frac{\left(R^2 - d^2\cos^2\sigma\right)^2}{R^2 - d^2}\dot{R}^2 = ER^2 + \mu R + C_1$$
$$\frac{1}{2}\left(R^2 - d^2\cos^2\sigma\right)^2\dot{\sigma}^2 = -Ed^2\cos^2\sigma + \mu\beta d\cos\sigma + C_2,$$

where $\mu = G(m_+ + m_-)$ and $\beta = \frac{m_+ - m_-}{m_+ + m_-}$, with d described above. It can be verified that $C_1 + C_2 = 0$. The constants are used to define the eccentricities of orbits. More will be explained below.

3.5. **Types of Orbits.** There are three types of orbits corresponding to the Euler Problem.

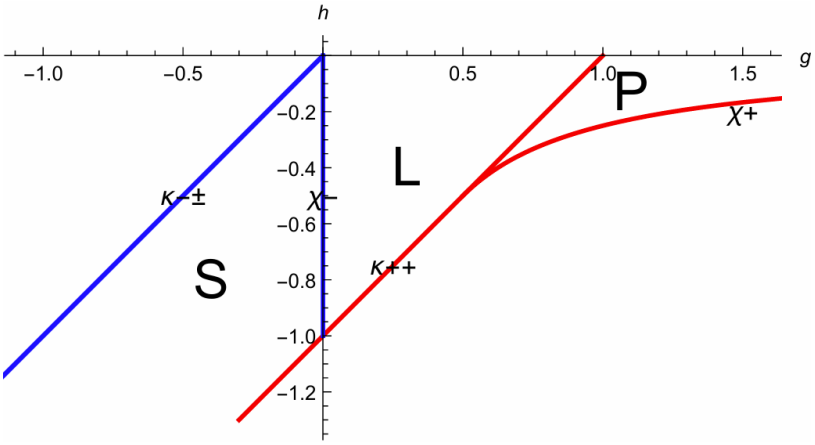

FIGURE 5. [4]. Three Types of Orbits. S refers to Satellite. L refers to Lemniscate. P refers to Planetary. h and g are from the section above.

3.5.1. *Satellite Orbit.* Below is the trajectory of a Satellite Orbit. The characteristic of this orbit is that the third body seems to never pass through the mid-point between the two fixed centers. This can be seen in Figure (6).

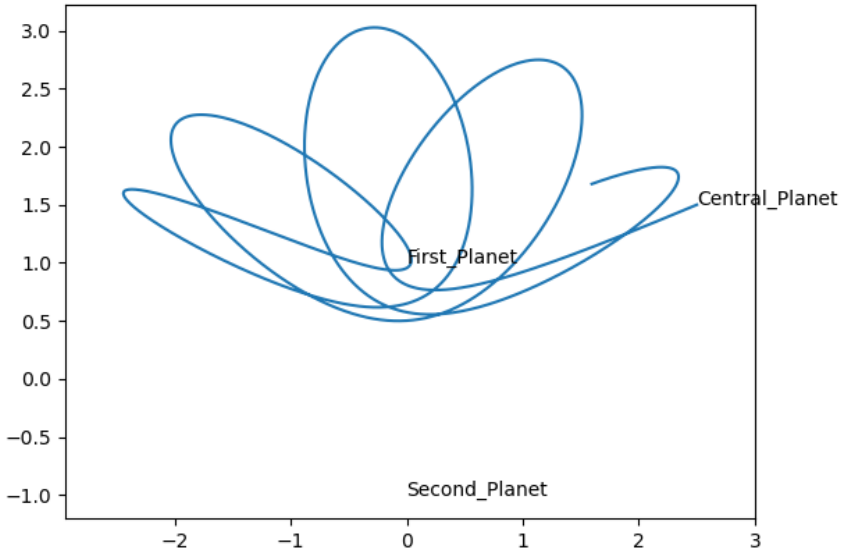

FIGURE 6. An example of a trajectory of the satellite orbit. This corresponds to a e value of 0.986. The g and h values are -0.522 and -0.734 respectively (definition of g and h can be seen in Figure (5)).

3.5.2. *Lemniscate Orbit.* The characteristic of a lemniscate orbit is that the third body passes through the line between the two fixed centers. This can be seen in Figure (6).

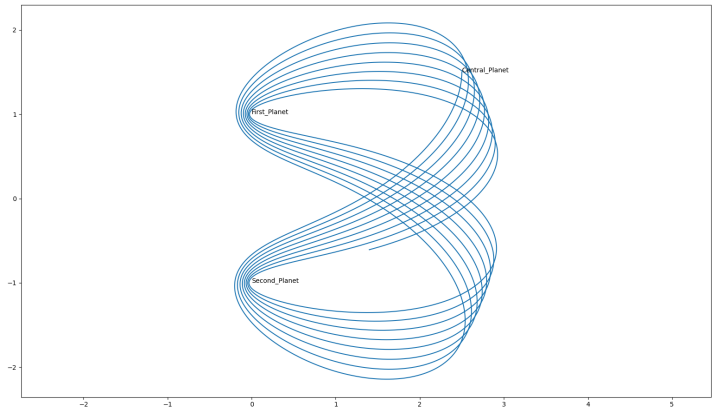

FIGURE 7. An example of a trajectory of the lemniscate orbit. The e value is 1.08. The g and h values are 0.173 and -0.739 respectively.

3.5.3. *Planetary Orbit.* The characteristic of a planetary orbit is that the third body *almost* forms a complete ellipse around the two centers. This is explained further below. Figure (8) shows an example of the trajectory.

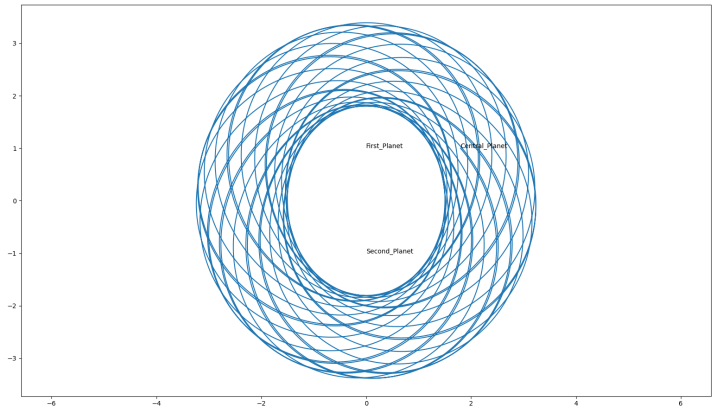

FIGURE 8. An example of a trajectory of the planetary orbit. This orbit has a e value of 2.56 (used below). The g and h values are 3.38 and -0.339 respectively.

3.6. **Textbook Verification.**

3.6.1. *Eccentricity and Semi-Major Axis of closed orbits.* Below we will verify results from the textbook *Integrable Systems in Celestial Bodies* [8].

First, we will define some constants.

We have:

$$C = \sqrt{2C_2}$$
$$p = \frac{C^2}{2}$$
$$a = -\frac{1}{E} \quad (E \text{ is total energy of the system})$$
$$e = \sqrt{1 - \frac{p}{a}}$$
$$\eta = \frac{1}{p}$$

3.6.2. *Graph for Eccentricities and Semi-Major Axes.* We will plot the graphs for all three types of orbits, and use the formulae above to find the eccentricities and semi-major axes corresponding to each orbit.

Type of Orbit	η	p
Planetary	0.425	2.35
Lemniscate	2.40	0.416
Satellite	4.34	0.231

TABLE 4. Types of orbits and their corresponding values of η

In the textbook, when $\eta^2 < 1$, it corresponds to a closed elliptic orbit of eccentricity η and semimajor axis p. Indeed the Planetary Orbit corresponds best to a closed elliptic orbit. This can be seen in Figure (9).

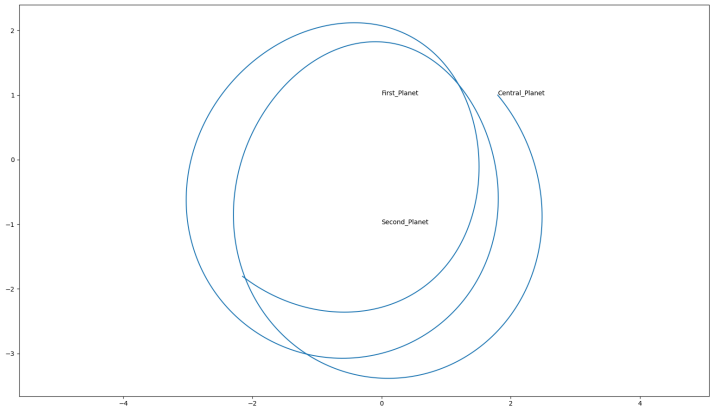

FIGURE 9. Planetary Orbit. It corresponds to a closed elliptic orbit.

We have found the semi-major axis for the first 5 orbits. As the two fixed centers are the foci of the ellipses, we can find the corresponding eccentricity also by:

$$\text{Eccentricity} = \frac{1}{\text{Semi-Major Axis}}$$

Orbit	Semi-Major Axis	Eccentricity
1st Orbit	2.60	0.384
2nd Orbit	2.60	0.385
2nd Orbit	2.57	0.390
3rd Orbit	2.63	0.381
4th Orbit	2.49	0.401
5th Orbit	2.26	0.443
Average	2.53	0.397
Theoretical Value	2.35	0.425

TABLE 5. Corresponding values of Semi-Major Axis and Eccentricity for each orbit.

As seen in Table (4), the theoretical values correspond well to the measured values.

3.6.3. *Plotting $S = \cos\sigma$ over time for $e^2 > 1$.* By setting $S = \cos\sigma$, the author obtained:

$$S'^2 = (1 - S^2)[1 - k_{01}^2 S^2]$$

For $e^2 > 1$, where e refers to eccentricity. This can be solved using Jacobi Elliptic Functions.

There are in total 12 types of Jacobi Elliptic Functions. This is summarized below:

Category	Functions
Primary functions	$\mathrm{sn}(u\|k)$, $\mathrm{cn}(u\|k)$, $\mathrm{dn}(u\|k)$
Reciprocal functions	$\mathrm{ns}(u\|k)$, $\mathrm{nc}(u\|k)$, $\mathrm{nd}(u\|k)$
Quotient functions	$\mathrm{sc}(u\|k)$, $\mathrm{sd}(u\|k)$, $\mathrm{cs}(u\|k)$, $\mathrm{cd}(u\|k)$, $\mathrm{ds}(u\|k)$, $\mathrm{dc}(u\|k)$

TABLE 6. Jacobi Elliptic Functions

We will only be concerned about the primary functions. Below is a table of its derivatives.

Function	Derivative
$\mathrm{sn}(u\|k)$	$\frac{d}{du}\mathrm{sn}(u\|k) = \mathrm{cn}(u\|k) \cdot \mathrm{dn}(u\|k)$
$\mathrm{cn}(u\|k)$	$\frac{d}{du}\mathrm{cn}(u\|k) = -\mathrm{sn}(u\|k) \cdot \mathrm{dn}(u\|k)$
$\mathrm{dn}(u\|k)$	$\frac{d}{du}\mathrm{dn}(u\|k) = -k^2\mathrm{sn}(u\|k) \cdot \mathrm{cn}(u\|k)$

TABLE 7. Derivatives of Primary Jacobi Elliptic Functions

Identity	Equation
Sum of squares of sn and cn	$\mathrm{sn}^2(u \mid k) + \mathrm{cn}^2(u \mid k) = 1$
Sum of squares of dn and sn	$\mathrm{dn}^2(u \mid k) + k^2\,\mathrm{sn}^2(u \mid k) = 1$

TABLE 8. Identities of Jacobi Elliptic Functions

We will show that $S = \mathrm{sn}(f + \omega \mid k_{01})$ solves the equation above.

We can obtain:

$$S'^2 = (\mathrm{cn}(f + \omega \mid k_{01})\,\mathrm{dn}(f + \omega \mid k_{01}))^2$$

Using these identities, we can express cn and dn in terms of S:

$$\mathrm{cn}(f+\omega \mid k_{01}) = \sqrt{1-\mathrm{sn}^2(f+\omega \mid k_{01})} = \sqrt{1-S^2}$$

$$\mathrm{dn}(f+\omega \mid k_{01}) = \sqrt{1-k_{01}^2\,\mathrm{sn}^2(f+\omega \mid k_{01})} = \sqrt{1-k_{01}^2 S^2}$$

By substitution,

$$S'^2 = \left(\sqrt{1-S^2}\cdot\sqrt{1-k_{01}^2 S^2}\right)^2$$

And therefore,

$$S'^2 = (1-S^2)(1-k_{01}^2 S^2)$$

Below is a graph of $\mathrm{sn}(u|k)$, given different values of k.

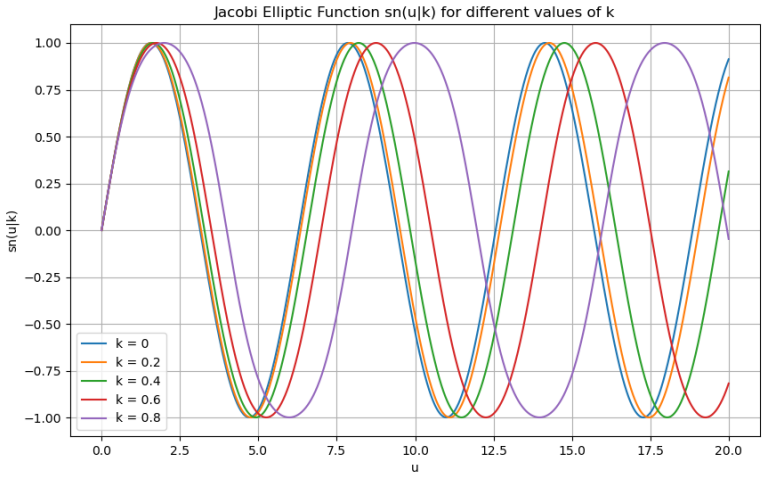

FIGURE 10. A graph of $sn(u|k)$ given different values of k.

It can be seen that in general, the S over time graph for different orbits roughly follows the shape of Sn. Note that it doesn't start at zero due to the constant ω.

As seen above, $e^2 > 1$ refers to Planetary and Lemniscate orbits. The S graphs for both orbits are shown below:

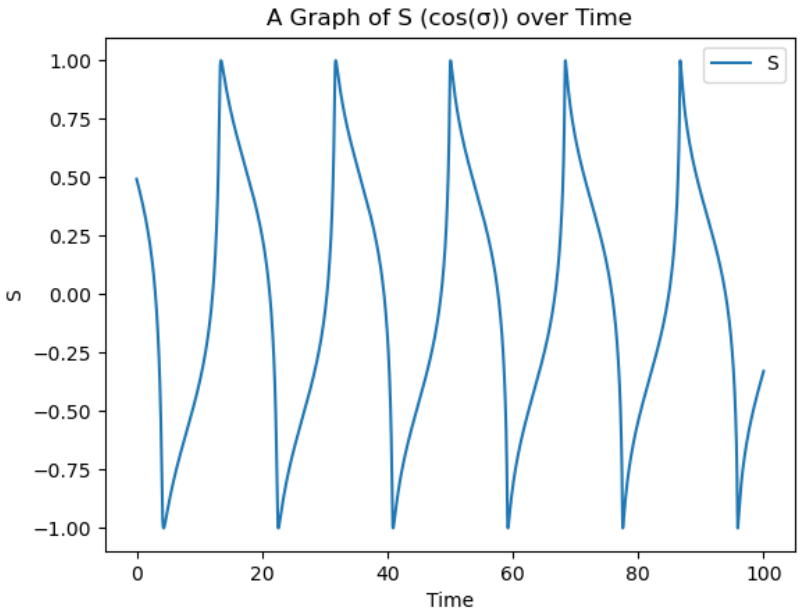

FIGURE 11. The S graph for a planetary orbit.

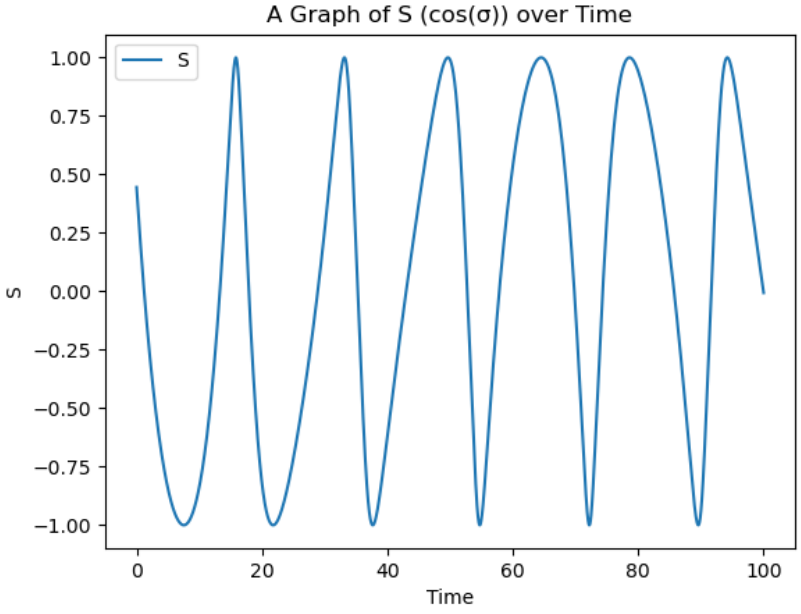

FIGURE 12. The S graph for a lemniscate orbit.

3.6.4. *Plotting $S = \cos\sigma$ over time for $e^2 < 1$.* For $e^2 < 1$, where e is the eccentricity, it is quite similar. The only difference is that we are solving

$$S'^2 = (1 - S^2)[1 - k_{02}^2(1 - S^2)$$

instead.
The reader can verify that

$$S = \mathrm{cn}[f + \Omega : k_{02}]$$

solves the equation above, where Ω is another constant.

The graphs of cn and sn are similar as they differ by only a constant phase.

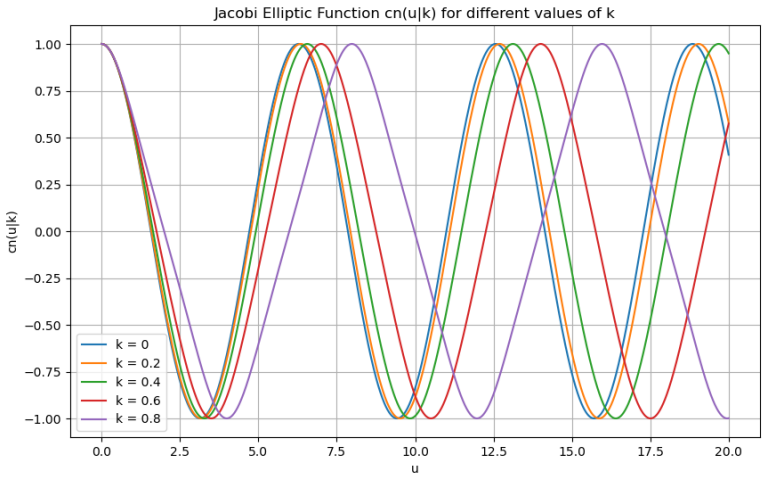

FIGURE 13. A graph of $cn(u|k)$ given different values of k.

$$e^2 < 1$$

refers to a Satellite Orbit. The corresponding S graph is shown below.

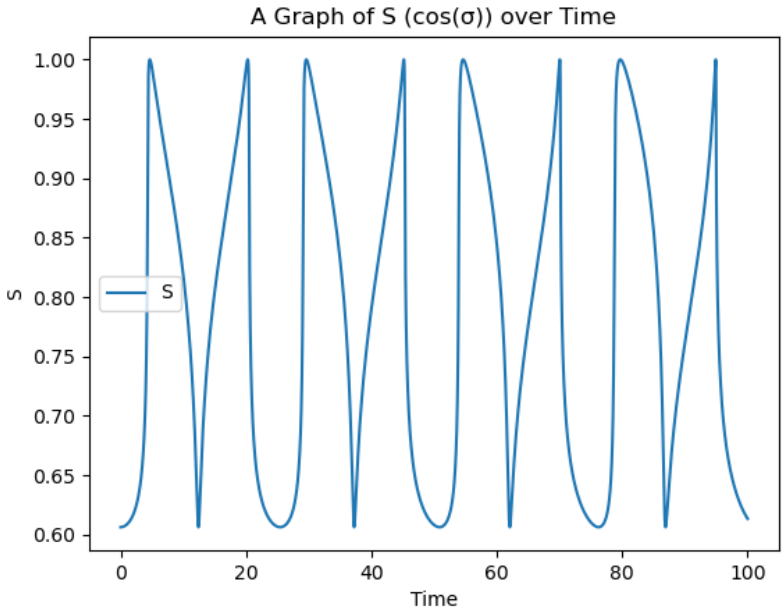

FIGURE 14. The S graph for a satellite orbit.

Notice that there are more frequent peaks for the Satellite orbit compared to Lemniscate and Planetary orbits. This implies in our specific examples, $k_{02} < k_{01}$.

3.7. **Errors in simulation for the Problem of Fixed Centers.** It has been found that the values of g and h are not constants in our simulation; they vary with time. Therefore, in the sections above, we merely take their averages. This may be due to inaccuracies in translating the formulae from the original paper, as the setup is slightly different. Another possible reason is an error in the Python code or a misunderstanding of the coordinate system used.

There are occasionally huge spikes for the values of C_1 and C_2. Therefore we only take the average of the first few values for our simulation. We speculate this is because the value of R can be close to 1, so the denominator $R^2 - d^2$ can be close to 0, which causes huge numerical instabilities.

4. Generalized Three-Body Problem

As we have explored the constrained three-body problem, it is time to solve the full three-body problem.

4.1. Lagrange Orbit.

4.1.1. *Lagrange Points.* Before we dive into the Lagrange Orbit, we will explore some theory of the Lagrange Points. For each two-body system, there exist 5 points of equilibrium, in which there is no net force on the third body. These points can be labelled from L_1 to L_5.

4.1.2. *Relation to the Lagrange Orbit.* Lagrange discovered the Lagrange Orbit in 1772. It is a family of solutions in which the three *equal* masses form an equilateral triangle at each instant [6]. The initial conditions can be visualized in Figure (15). In fact, the third point mass lies either on L_4 or L_5. The trajectory of the Lagrange Orbit can be seen in Figure (16).

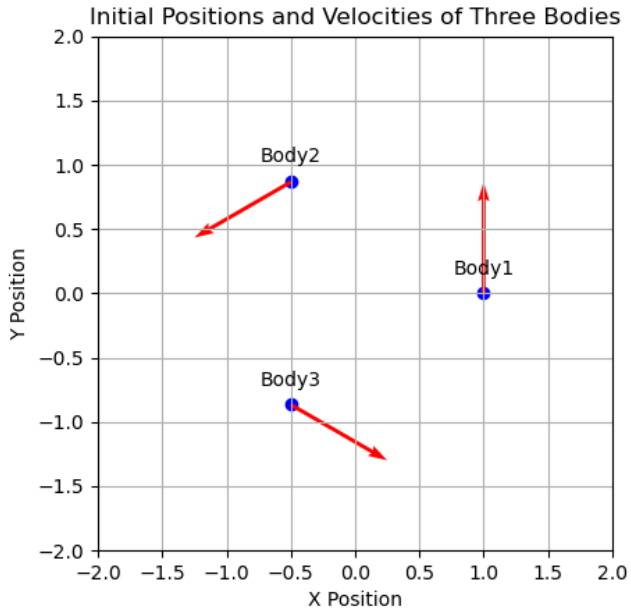

Figure 15. The initial positions of a Lagrange Orbit. The arrows denote the magnitude and directions of the velocity vectors.

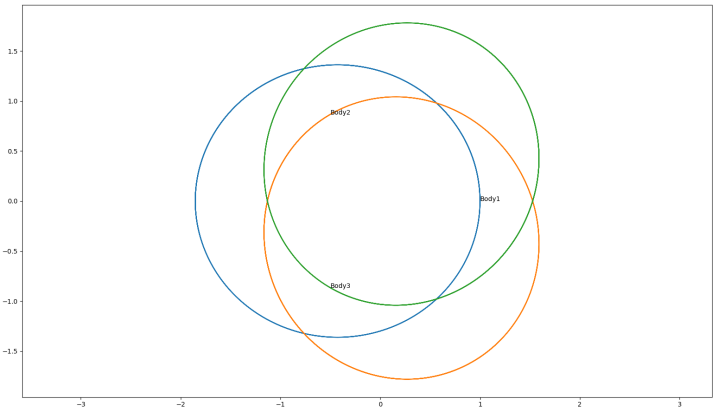

FIGURE 16. The trajectory of a Lagrange Orbit.

It has been shown that L_4 and L_5 are stable equilibria, provided $\frac{M_1}{M_2} > 24.96$ [10]. However, we assume the three masses to be identical, so both L_4 and L_5 are unstable in our case.

Therefore while simulating the results over a long period, the bodies deviate from the original path. This can be seen in Figure (17).

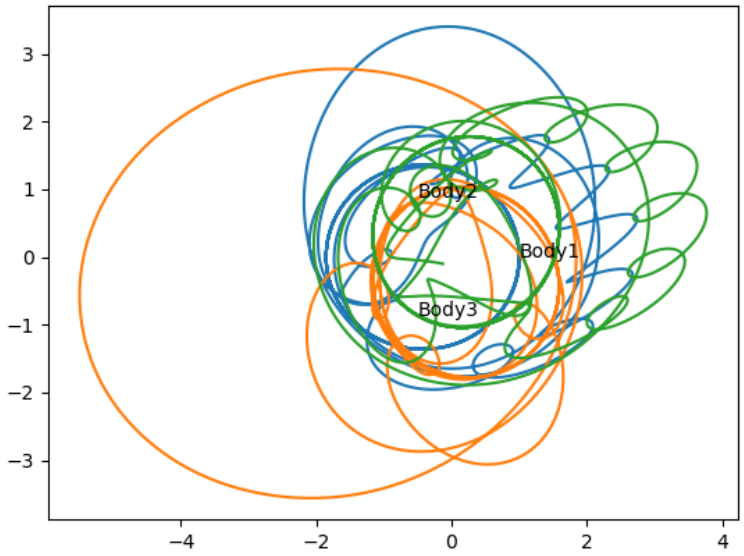

FIGURE 17. The trajectory of a Lagrange Orbit over a long simulation period. It deviates from the original orbit significantly. This is due to the unstable nature of the orbit.

4.2. **Figure-8 Orbit.** The Figure-8 Orbit was discovered in 1993, by C. Moore [7]. The initial conditions can be seen in Figure (18).

This orbit is highly symmetric, as the second and third bodies appear to have the same trajectory as the first body, except for a different phase. This can be seen in Figure (19).

Unlike the Lagrange Orbit, this orbit is stable. This will be shown in one of the sections below. A slight perturbation will not cause the bodies to fly off; instead, the resultant trajectory deviates only slightly from the original orbit. This can be seen in Figure (20).

The proof of the figure-8 orbit is neat and will be presented in the next section.

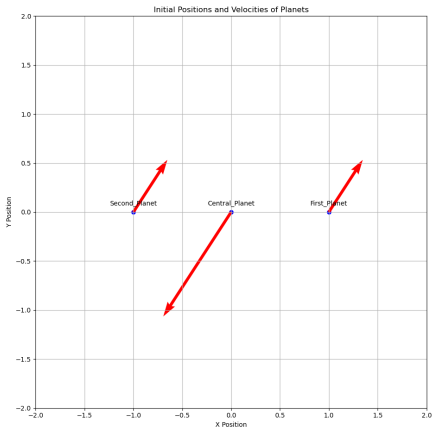

FIGURE 18. The initial positions of a Lagrange Orbit. The arrows denote the magnitude and directions of the velocity vectors.

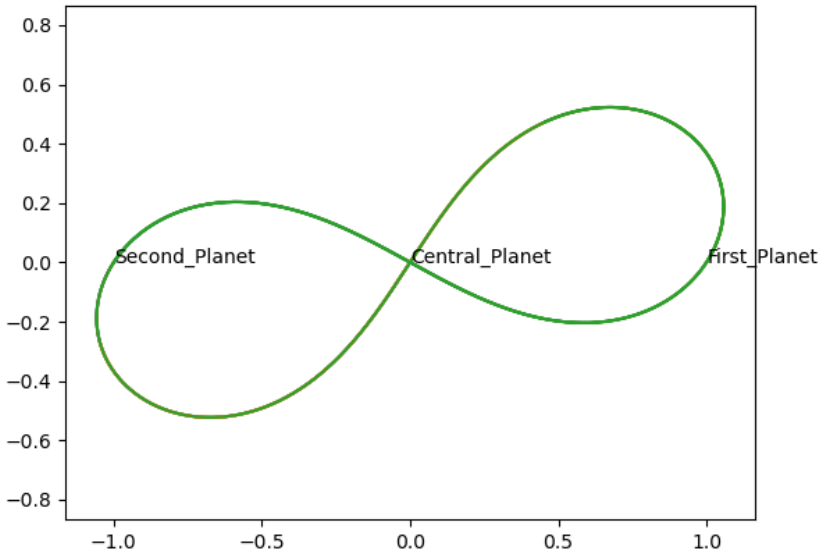

FIGURE 19. The Figure-8 Orbit Trajectory.

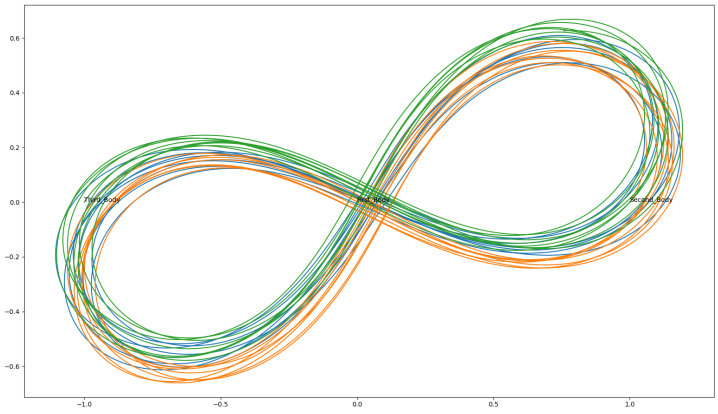

FIGURE 20. The Figure-8 Orbit Trajectory, under a small perturbation.

4.3. **BHH Orbit.**

4.3.1. *Jacobi Coordinates.* In a three-body problem, the bodies act on each other based on gravitational forces. Therefore, the effect of translation can be excluded [3].

In other words, consider X to be the coordinates of the sets of orbits we will consider.

$$X = \left\{ x = (x_1, x_2, x_3) \in \mathbb{C}^3 \mid \sum_{i=1}^{3} x_i = 0 \right\}.$$

Where x_1 are the coordinates of the first body, x_2 are the coordinates of the second body, etc.

With this in mind, we introduce the Jacobi Coordinates, which is defined as [9]:

$$(\rho, \lambda) = \left(r_2 - r_1, \frac{2r_3 - r_1 - r_2}{\sqrt{3}} \right)$$

This is a mapping from X to $\mathbb{C}^2$. ρ describes the relative position of m_2 in terms of m_1. λ describes the position of the m_3 relative to a combination of the first two.

4.3.2. *Relation to BHH Orbit.* In the BHH Orbit, the particles have $(x_1, 0, 0), (x_2, 0, 0), (x_3, 0, 0)$ as initial positions, and $(0, v_{y1}, 0), (0, v_{y2}, 0), (0, v_{y3}, 0)$ as initial velocities.

Then, the coordinates, a to d, are defined as [9]:

$$\begin{aligned} a &= \frac{x_1 - x_2}{\sqrt{2}} \\ c &= \frac{v_{y1} - v_{y2}}{\sqrt{2}} \\ b &= \frac{x_1 + x_2 - 2x_3}{\sqrt{6}} = 1 \\ d &= \frac{v_{y1} + v_{y2} - 2v_{y3}}{\sqrt{6}} = L - ac \end{aligned}$$

We now aim to find the initial positions and velocities given a, c and L.

We can also express:

$$x_1 - x_2 = a\sqrt{2}$$
$$x_1 + x_2 - 2x_3 = \sqrt{6}$$

which can be simplified to:

$$x_1 - x_2 = a\sqrt{2}$$
$$x_1 + x_2 = \sqrt{6}$$

By taking $x_3 = 0$.

Hence $x_1 = \frac{\sqrt{6}+a\sqrt{2}}{2}$ and $x_2 = \frac{\sqrt{6}-a\sqrt{2}}{2}$.

Similarly,

$$v_{y1} - v_{y2} = c\sqrt{2}$$
$$v_{y1} + v_{y2} - 2v_{y3} = d\sqrt{6}$$

Again, by assuming $v_{y3} = 0$, we obtain:

$$v_{y1} - v_{y2} = c\sqrt{2}$$
$$v_{y1} + v_{y2} = d\sqrt{6}$$

Hence $v_{y1} = \frac{c\sqrt{2}+d\sqrt{6}}{2}$ and $v_{y2} = \frac{d\sqrt{6}-c\sqrt{2}}{2}$.

To summarise, we have:

$$(x_1, x_2, x_3) = \left(\frac{\sqrt{6}+a\sqrt{2}}{2}, \frac{\sqrt{6}-a\sqrt{2}}{2}, 0\right)$$
$$(v_{y1}, v_{y2}, v_{y3}) = \left(\frac{c\sqrt{2}+(L-ac)\sqrt{6}}{2}, \frac{(L-ac)\sqrt{6}-c\sqrt{2}}{2}, 0\right)$$

4.3.3. *Trajectories of BHH Orbits.* The characteristic of a BHH orbit is that two bodies appear to be more involved than the third body. This can be seen in Figure (21). The corresponding initial conditions are shown in Figure (22).

Unfortunately, this trajectory differs from the theoretical trajectory. The possible reasons are:

- Incorrect assumptions that x_3, $v_{y3} = 0$.
- Inaccurate numerical method. This can be solved by using numerical methods of higher order, but this results in a much higher running time.

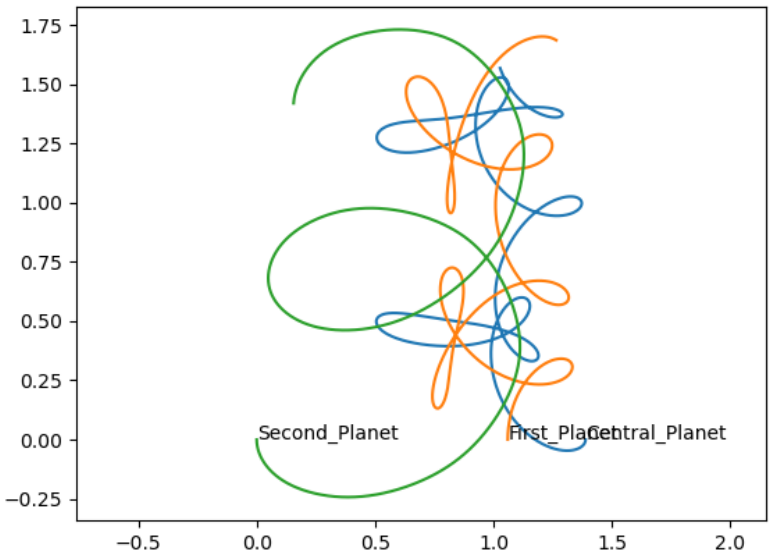

FIGURE 21. The trajectories of a BHH Orbit. This is only one of the many possible BHH orbits, corresponding to $a = 0.232402133831$, $c = -1.514749892810$, $L = 0.9355489170$.

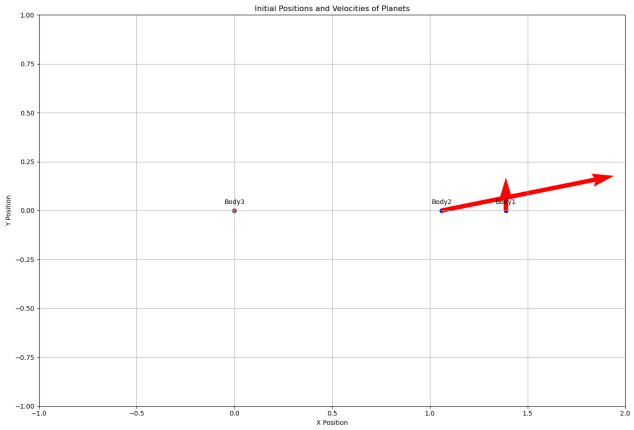

FIGURE 22. The initial conditions of the BHH Orbit.

4.4. **Shape Sphere.** This section is based on the paper *A remarkable periodic solution of the three-body problem in the case of equal masses* [3].

4.4.1. *Setup and Examples.* We mentioned above we can remove the effect of *translation*. This is a mapping from $\mathbb{C}^3$ to X.

The Jacobi coordinates mapped X to $\mathbb{C}^2$.

It is convenient if we can map $\mathbb{C}^2$ to $\mathbb{R}^3$ as we can then rescale and plot it on a unit sphere.

This resultant sphere is named the "shape sphere", and is documented in the paper *A remarkable periodic solution of the three-body problem in the case of equal masses.*

In that paper, the Jacobi coordinates have a slightly different notation:

$$(z_1, z_2) = \mathcal{J}(x_1, x_2, x_3) = \left(\frac{1}{\sqrt{2}} (x_3 - x_2), \sqrt{\frac{2}{3}} \left(x_1 - \frac{1}{2} (x_2 + x_3) \right) \right).$$

This is very similar to (ρ, λ) above, except that the order of 1, 2, and 3 are interchanged, and the scaling factors are different. We then define the Hoft map:

$$\mathcal{K} : \mathbb{C}^2 \to \mathbb{R} \times \mathbb{C} \cong \mathbb{R}^3$$

specified by:

$$\mathcal{K}(z_1, z_2) = (u_1, u_2 + iu_3) = \left(|z_1|^2 - |z_2|^2, 2\bar{z}_1 z_2 \right).$$

This is related to *Hopf Fibration* in Differential Topology. The intuition and formulation of this mapping are omitted.

Each point on the shape sphere corresponds to a particular formulation of the three bodies.

Example 1. E_1, E_2, and E_3 refer to the collinear configurations in the three-body problem where one of the bodies sits at the midpoint of the segment defined by the other two. Each configuration is distinguished by which mass is at the midpoint. The coordinates of E_1 to E_3 are:

$$E_1 = (1, 0, 0), \quad E_2 = \left(-\frac{1}{2}, -\frac{\sqrt{3}}{2}, 0 \right), \quad E_3 = \left(-\frac{1}{2}, \frac{\sqrt{3}}{2}, 0 \right)$$

Example 2. M_1, M_2, and M_3 refer to specific isosceles configurations in the three-body problem where two of the bodies are equidistant, and the third body is positioned uniquely. Each configuration is distinguished by which mass forms the unique position.

M_i is a line on the sphere that runs from E_i to its antipodal collision point C_i, which are positions on the sphere opposite to E_i.

Example 3. The equilateral triangle formulation corresponds to $L_\pm$. They are located at $(0, 0, 1)$ and $(0, 0, -1)$ respectively.

4.4.2. *Plots.* The trajectories of the Figure-8 Orbit, Lagrange Orbit, and the BHH Orbit on the shape sphere are presented.

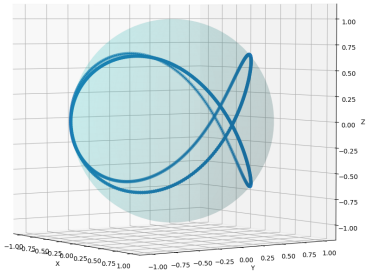

FIGURE 23. The Figure-8 Orbit on the shape sphere

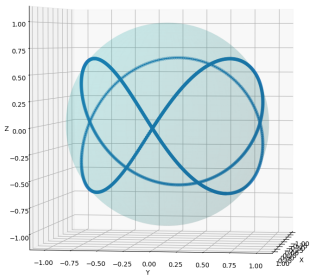

FIGURE 24. The Figure-8 Orbit on the shape sphere, viewed from another angle.

As the Lagrange Orbit form an equilateral triangle at each instant, the shape sphere coordinates are expected to be at $L_{\pm}$, *i.e.* $(0, 0, 1)$ or $(0, 0, -1)$.

This is confirmed in the plot, where all the points are located around $(0, 0, 1)$, *i.e.* at L_{+}.

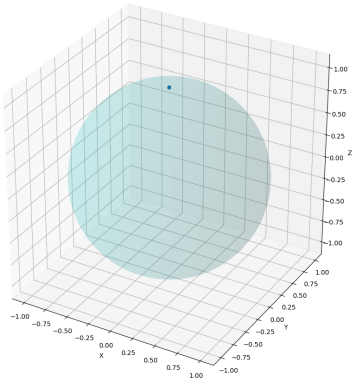

FIGURE 25. The Lagrange Orbit on the shape sphere. It may be hard to see, but the points lie around $(0, 0, 1)$.

The BHH orbit on the shape sphere differs from the theoretical trajectory. The possible reasons are listed above.

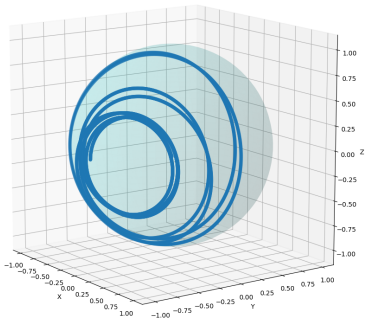

FIGURE 26. The BHH Orbit on the shape sphere.

5. Proof of Existence of Figure-8 Orbit

In this section, we will attempt to form analytical proof of the Figure-8 Orbit. Before this, we will state the principle of least action, which is the key to the proof. Same as above, this section is based on the paper *A remarkable periodic solution of the three-body problem in the case of equal masses* [3].

5.1. Definition of Action and Principle of Least Action.

The Action can be defined as the integral of tThe Lagrangian from, say, $t = a$ to $t = b$. Here, we are concerned about orbits from $t = 0$ to $t = T$. Hence, it can be expressed as:

$$\mathcal{S}(m_1, m_2, m_3; x) = \int_0^T \left(\frac{1}{2} \sum_{i=1}^{3} m_i \left| \dot{x}_i(t) \right|^2 + \sum_{1 \le i < j \le 3} \frac{m_i m_j}{|x_j(t) - x_i(t)|} \right) dt.$$

With this in mind, we can define the Principle of Least Action.

Definition 1. The Principle of Least Action states that the actual path taken by an object makes the action stationary. In other words, it satisfies:

$$\delta S = 0$$

A path that satisfies this condition is called a minimizer.

5.2. **Structure of the Proof.**

- **In the shape-sphere space**, find minimizers travelling from E_3 to M_1 (Definitions of both E_3 and M_1 are in the section above). This corresponds to 1/12th of the full orbit.
- Showing such a path has no collisions.
- Extend the path mentioned above 12 times (through copy and paste) until a whole continuous orbit is formed.
- Argue that this shape in the shape sphere would form a Figure-8 Orbit.

5.3. **Showing a minimizer from E_3 to M_1 exists and the path has no collision.** The existence of a minimizer is trivial as the space of admissible paths is compact. The difficulty is to prove the path has no collisions.

The distance from E_3 to M_1 is denoted as l_0. It can be shown that $l_0 < \frac{\pi}{5}$. It is proved that if $l_0 < \frac{\pi}{5}$, The minimum of the actions of equipotential test paths is smaller than A_2, the infimum of the actions of collision paths in time T. However, it can also be shown that if the path contains a double or triple collision, its minimum action is greater than A_2. This shows that our path does not contain collisions.

5.4. **Proving the path is smooth and continuous after *copy and pasting*.** If we can show at all endpoints, $\frac{\partial \mathcal{L}}{\partial \dot{x}}$ points out of the sphere, then the whole orbit is continuous.

Assume $\epsilon\eta(t)$ is an infinitesimally small deviation from the path on the sphere, where $\eta(t)$ is a tangent vector to the surface of the sphere. Inserting this into the standard proof of the Euler–Lagrange equation, we have:

$$\delta A = \epsilon \left[\frac{\partial \mathcal{L}}{\partial \dot{x}} \eta \right]_0^T + \epsilon \left[\int_0^T \left(\frac{\partial \mathcal{L}}{\partial x} - \frac{d}{dt} \frac{\partial \mathcal{L}}{\partial \dot{x}} \right) \eta \, dt \right]$$

The terms in the bracket should independently go to zero. For this proof, we will only consider the first term.

This requires $\frac{\partial \mathcal{L}}{\partial \dot{x}}$ to be orthogonal to the tangent plane of the manifolds at the endpoints. Hence $\frac{\partial \mathcal{L}}{\partial \dot{x}}$ acts as a normal vector of the sphere at all endpoints.

5.5. **The Area Rule and showing the three bodies only differ by a phase.**

Definition 2. The *Area Rule* states that the angle of rotation of the symmetric axis is equal to twice the area enclosed by the shape curve.

As seen in Figure (27), while travelling from E_3 to E_1, the total enclosed area is zero. This reflects why the line joining m_1, m_2 and m_3 are fixed.

While travelling from M_1 to M_1 (recall that M_1 means $r_{12} = r_{13}$), the total enclosed area is also zero. Therefore, the symmetric axis of the triangle is not changed.

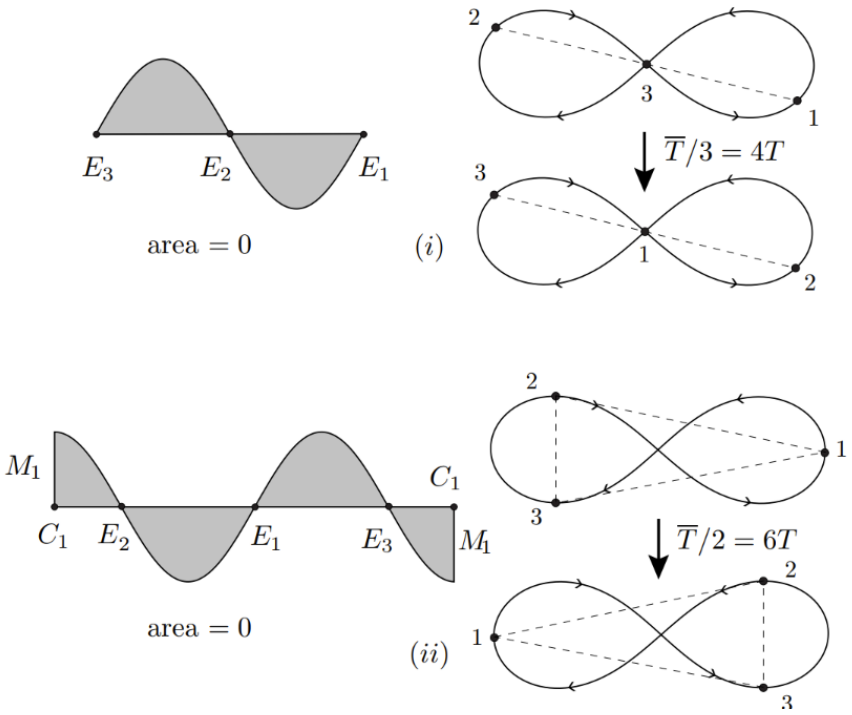

FIGURE 27. An illustration of the area enclosed by the shape curve.

The first scenario corresponds to $0 \leq t \leq \bar{T}/3$. It can be seen that the three bodies only differ by a phase of $\bar{T}/3$. In other words, by setting $q(t) = x_3(t)$ where $x(t) = (x_1(t), x_2(t), x_3(t)$. In other words,

$$\begin{cases} q(t) = x_3(t) \quad \text{for } 0 \leq t \leq \dfrac{\bar{T}}{3}, \\ q(t) = x_2\left(t - \dfrac{T}{3}\right) \quad \text{for } \dfrac{\bar{T}}{3} \leq t \leq \dfrac{2\bar{T}}{3}, \\ q(t) = x_1\left(t - \dfrac{2\bar{T}}{3}\right) \quad \text{for } \dfrac{2\bar{T}}{3} \leq t \leq \bar{T}. \end{cases}$$

5.6. **Showing extra loops cannot occur.** The final step is to show that any extra loops cannot occur.

The proof involves measuring the particles in polar coordinates, *i.e.* in terms of (r, θ)

It can be shown that the angular momentum for each particle remains strictly negative for $0 < t < \bar{T}/2$. As the angular momentum is proportional to $r^2\dot{\theta}$, $\dot{\theta}$ is negative, and hence θ strictly decreases. This cannot happen for an orbit with extra loops.

Therefore loops cannot occur in this orbit.

5.7. **Concluding that the orbit is a Figure-8 Orbit.** Based on the above sections, it can be concluded that the Figure-8 orbit is the only orbit that satisfies the above properties. Details of the proof can be found in the original paper.

6. Exploring Sundman's Series

Karl Fritiof Sundman showed that there exists an analytic solution to the Three-Body Problem, in powers of $t^{1/3}$, subject to some constraints. The proof is very long and tedious, so we will only present its convergence region and rate here. This section

is mainly based on the paper *Exposition of Sundman's regularization of the three-body problem* [13].

6.1. **Singularities in Double and Triple Collisions.** To form Sundman's Series, a technique named *regularization* is used. This means adjusting variables which have singularities to make the values finite. Using this technique, the singularities for double collisions can be excluded. However, the singularities for triple collisions cannot be excluded. Therefore we attempt to find the conditions under which triple collisions will occur.

Sunmdan showed that when triple collisions require $\mathbf{c} = 0$, where $\mathbf{c}$ is equal to:

$$m_0(\mathbf{r_0} \times \mathbf{v_0}) + m_1(\mathbf{r_1} \times \mathbf{v_1}) + m_2(\mathbf{r_2} \times \mathbf{v_2}) = \mathbf{c}$$

This is indeed the sum of angular momentum. Note that the Figure-8 Orbit from above has zero angular momentum, and hence cannot be expressed by Sundman's series.

6.2. **Convergence of Sundman's Series.**

6.2.1. *Definition of w.* We define:

$$dt = \Gamma dw$$

with the initial conditions $w = 0$ when $t = 0$.

Where Γ can be defined as:

$$\Gamma = (1 - e^{\frac{-r_0}{l}})(1 - e^{\frac{-r_1}{l}})(1 - e^{\frac{-r_2}{l}})$$

The symmetry of this setup causes r_0 to be indistinguishable from r_1 and r_2. Hence any combination of double collisions can occur.

6.2.2. *Convergence Strip.* We arrive at $|w - \bar{w}| < \Omega$, where Ω is real and $\bar{w}$ is the value of w when $t \to \bar{t}$. Since $\bar{w} \in \mathbb{R}$, the convergent discs have centers on the real line. Therefore, the convergent region is a strip of width 2Ω. This can be seen in the figure below, where the orange circles have a radius Ω.

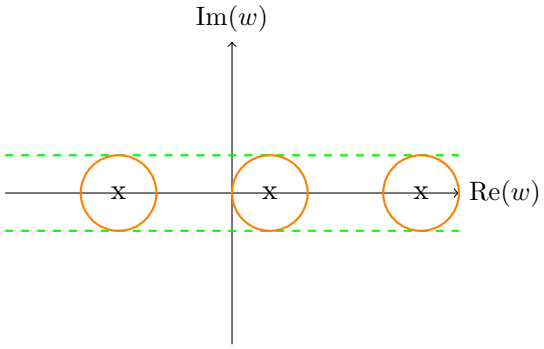

In power series, the convention is to express the *convergence region* as a disc. This can be done using Möbius Transformation in Complex Analysis.

We can denote the strip as: $S = [s : \mathrm{Im}(s) \leq \beta]$, where β is Ω from above. This is the convention used in the book.

6.3. **Mapping a Convergence Strip to a Unit Disc using Möbius Transformation.** First, notice that $g(z) = e^{\frac{\pi s}{2\beta}}$ maps S to the right half-plane.

Next, notice that for the right half-plane, $|z-1| < |z+1|$. This implies $h(z) = \frac{|z-1|}{|z+1|} < 1$ maps the right half-plane to the unit disc. $h(g(z))$ thus maps S to the unit disc centered at the origin.

This implies that:

$$\tau = \frac{e^{\frac{\pi s}{2\beta}} - 1}{e^{\frac{\pi s}{2\beta}} + 1}$$

maps the convergence strip to the unit disc centred at the origin.
Alternatively, this can be expressed as:

$$s = \frac{2\beta}{\pi} \log \frac{1+\tau}{1-\tau}$$

It is also known that $s \propto t^{1/3}$. Therefore it can also be expressed as:

$$\tau = \frac{e^{\alpha t^{1/3}} - 1}{e^{\alpha t^{1/3}} + 1}$$

where α is a constant. The proof is omitted.

6.4. **Showing Sundman's Series has Slow Convergence.** This subsection is based on the analysis of Belorizky [1]. Consider the Lagrange Orbit. As we showed above, each orbit has a circular path. Thus, it can be parameterized as:

$$(x, y) = (\cos(t), \sin(t)).$$

From the previous post, we can see that:

$$\Gamma = (1 - e^{\frac{1}{l}})^3$$

As $t = \Gamma w$, we can see:

$$t = \frac{2\beta\Gamma}{\pi} \log \frac{1+\tau}{1-\tau}$$

Using Taylor Expansion, this can be approximated as:

$$t = \frac{4\beta\Gamma}{\pi}(\tau + \frac{\tau^3}{3} + \frac{\tau^5}{5} + O(\tau^6))$$

Now consider the case where $m_1 = m_0$ and $m_2 = 1 - 2m_0$.
This implies:

$$(m_0, m_1, m_2) = (m_0, m_0, 1 - 2m_0).$$

Take $m_1 = \frac{1}{200}$. This corresponds to :

$$\beta < 9 \times 10^{-8}.$$

Letting $\frac{4\Omega\Gamma}{\pi}$ as A, this corresponds to:

$$A < 4 \times 10^{-8}.$$

Now consider $t = 1$, *i.e.*

$$1 = \frac{4\beta\Gamma}{\pi}(\tau + \frac{\tau^3}{3} + \frac{\tau^5}{5} + O(\tau^6)).$$

For a one-decimal accuracy, we want:

$$\sum_{k=1}^{n} \left(\frac{4\beta\Gamma}{\pi}\right) \left(\frac{\tau^{2k-1}}{2k-1}\right) > 0.9$$

We have:

$$S_\tau = \sum_{k=1}^{n} \frac{\tau^{2k-1}}{2k-1} > \frac{9}{20A}$$

The reader can show that $A < 4 \times 10^{-8}$ corresponds to $S_\tau > 10^7$.

Now relate this to the series:

$$S = \sum_{k=1}^{n} \frac{1}{2k-1}$$

It has been shown that $n > e^{2S-2.4}$.

Since $|\tau| < 1$, our series converges even slower. Hence we need even more terms. Therefore, $n > 10^{8\times 10^6}$. This shows the Sundman series converges too slowly and is very impractical to use.

7. Searching for Well-Behaved Orbits

Well-behaved orbits refer to orbits with energy deviation less than 1. We are attempting to find well-behaved orbits in the symmetric case with zero momentum. We have noticed that in non-well-behaved orbits, usually two bodies become too close to each other which breaks the simulation.

We now assume the first and third body have a starting position of $(-1, 0)$ and a starting velocity (a, b), whereas the second body has a starting position of $(0, 0)$ and a starting velocity of $(-2a, -2b)$, Notice that $a = 0.35, b = 0.53$ roughly corresponds to the Figure-8 Orbit. Now we vary a and b *both* from 0 to 1 and find the orbits with energy deviation less than 1. The assumption I have made in the simulation is that unbounded orbits correspond to a non-well-behaved orbit. This is not necessarily true but it is very effective in reducing computational time.

7.1. Preliminary Results.

The results are shown in Figure (28), where the x-axis denotes a and the y-axis denotes b. It can be seen that the Figure-8 Orbit has an energy deviation less than 1, as expected.

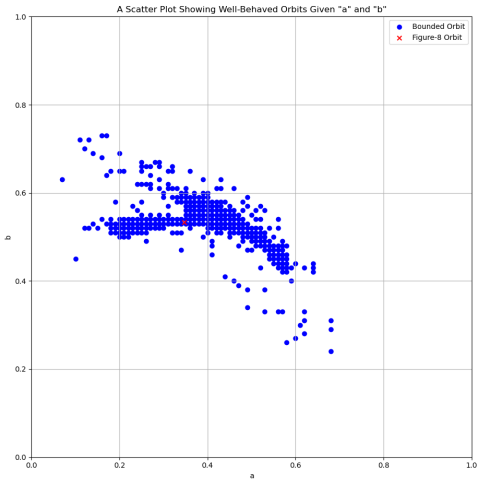

Figure 28. A plot plotting b against a. The blue dots correspond to a and b which causes the orbit to be well-behaved. The red cross denotes the orbit for Figure-8.

We can also notice that the Figure-8 Orbit is more stable in the x- direction than the y- direction. This is shown in Figure (29). Note that this is a close-up view of Figure (28) near the a and b corresponding to the Figure-8 Orbit.

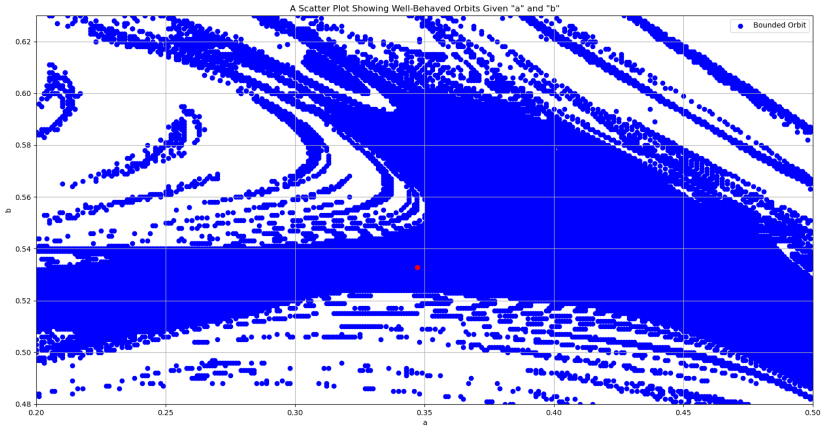

FIGURE 29. A close-up view of the region of a and b surrounding the a and b corresponding to the Figure-8 Orbit.

8. Conclusion

In this report, we explored both the numerical and theoretical complexities of the Three-Body Gravitational Problem. We introduced various interesting orbits and verified significant results through simulations, by picking the Neri algorithm as the integration method. An attempt has also been made to search for well-behaved orbits.

While significant progress has been made in classifying and understanding various orbits, the Three-Body Problem remains a promising ground for research, especially in the fields of computational physics and chaos theory.

This project contains extensive coding. The majority of the code is available for viewing in my GitHub repository. Any remaining code can be provided upon request.

9. Acknowledgments

I would like to express my gratitude to Dr. Jenni Smillie for generously taking the time to supervise this project. I am also thankful to the *School of Physics and Astronomy, University of Edinburgh* for funding this project. Additionally, I would like to thank Allison Lau (University of Toronto) for her encouraging comments.

10. Personal Statement

This project improved my communication skills drastically, especially during weekly meetings where I had to present what I had done over the past week. Up until this point in my degree, there have not been any group projects, therefore I am not too used to presenting my work verbally. This skill is vital for a physicist as collaborative work is ubiquitous, and being able to digest and implement others' suggestions will make me a catalyst in a group setting.

Using Python in a research setting also improved my programming skills significantly, as compared with coursework, where I complete small checkpoints sequentially. For example, I often had to figure out a new, previously unheard-of technique to approach a particular problem, while the general approach is given in coursework. Being proficient in programming will hopefully bring me closer to my goal of becoming a theoretical physicist.

11. Lay Summary

In courses such as Introductory Dynamics/Dynamics and Vector Calculus, the two-body problem has been explored, which leads to Kepler's three laws. This is a special case in the general N-body Problem, where an arbitrary number of bodies act on each other by Newton's inverse square gravitational law.

In this project, we approach the three-body problem. It is much more complicated and generally unsolvable, other than some special cases. In this project, we explored those special cases, which involve two bodies being fixed, and three bodies chasing the orbits of each other (Figure-8 Orbit).

Besides, we attempt to prove the existence of the Figure-8 orbit, as well as understand why currently existing analytical solutions cannot be used realistically.

Understanding the three-body problem will lead to a better understanding of the helium atom (which involves a helium nucleus and two electrons), as well as thermodynamics, and even general relativity.

References

[1] D Belorizky. "Application pratique des méthodes de M. Sundman à un cas particulier du problème des trois corps". In: *Bulletin Astronomique, vol. 6, pp. 417-434* 6 (1930), pp. 417–434.

[2] Rory Michael Casey. "Computer Implementation of Symplectic Integrators and Their Applications to the N-Body Problem". MA thesis. The University of North Carolina at Charlotte, 2020.

[3] Alain Chenciner and Richard Montgomery. "A remarkable periodic solution of the three-body problem in the case of equal masses". In: *Annals of Mathematics* (2000), pp. 881–901.

[4] Holger R Dullin and Richard Montgomery. "Syzygies in the two center problem". In: *Nonlinearity* 29.4 (2016), p. 1212.

[5] Des Higham. *Numerical Ordinary Differential Equations and Applications*. Lecture Notes. Based on notes previously prepared by several colleagues. School of Mathematics, University of Edinburgh, 2024.

[6] Wang Sang Koon et al. "Dynamical systems, the three-body problem and space mission design". In: *Equadiff 99: (In 2 Volumes)*. World Scientific, 2000, pp. 1167–1181.

[7] Christopher Moore. "Braids in classical gravity". In: *Phys. Rev. Lett* 70.24 (1993), pp. 3675–3679.

[8] Diarmuid Ó'Mathúna. *Integrable systems in celestial mechanics*. Vol. 51. Springer Science & Business Media, 2008.

[9] Institute of Physics Belgrade. *Three-Body Problem*. http://three-body.ipb.ac.rs/info.php. Accessed: 2024-08-14.

[10] Lina A Shalby and Noha A Ali. "The behavior of a satellite trajectory near the equilibrium points of Sun-Earth system and its control". In: *Theoretical and Applied Mechanics* 00 (2023), pp. 3–3.

[11] Jenni Smillie. *Lagrangian Dynamics Lecture Notes*. Lecture Notes. 2023.

[12] Milovan Šuvakov and V Dmitrašinović. "A guide to hunting periodic three-body orbits". In: *American Journal of Physics* 82.6 (2014), pp. 609–619.

[13] DK YEOMANS. "Exposition of SUNDMAN'S regularization of the three-body problem(Equations of motion and integrals of motion derived for Sundman regularization of three- body problem)". In: (1966).

[14] Joe Zuntz. *Solar System: Background Computer Modelling*. PDF. Accessed on 13/8/2024. 2023.